Materials Science & Engineering A 876 (2023) 145146

Contents lists available at ScienceDirect

Materials Science & Engineering A

journal homepage: www.elsevier.com/locate/msea

A high-entropy alloy syntactic foam with exceptional cryogenic and dynamic properties

Jin Meng [a,b], Yu Qiao [a,c], Yan Chen [a,b,**], Tian-Wei Liu [a], Tong Li [a,b], Hai-Ying Wang [a,b], Lan-Hong Dai [a,b,*]

[a] State Key Laboratory of Nonlinear Mechanics, Institute of Mechanics, Chinese Academy of Sciences (CAS), Beijing, 100190, PR China
[b] School of Engineering Science, University of Chinese Academy of Sciences, Beijing, 101408, PR China
[c] CAS Key Laboratory of Mechanical Behavior and Design of Materials, Department of Modern Mechanics, University of Science and Technology of China, Hefei, 230027, PR China

ARTICLE INFO

Keywords:
High entropy alloy
Metal foams
Energy absorption
Cryogenic
Shear band
High strain rate

ABSTRACT

Metal foams are in great demand in extreme service environments with cryogenic temperatures and high strain rates due to their unique properties. However, the reduced ductility and impact toughness under such conditions limit their applications. In this work, we tested the quasi-static and dynamic compression properties of CoCrFeMnNi high entropy alloy syntactic foam at liquid nitrogen temperature (−196 °C). We found that it exhibits ultra-high strengths and energy absorption capacity, especially a superior resistance to embrittlement at cryogenic temperature. Microstructural characterizations reveal that the foam matrix has a high twinning activity and shear localization propensity in cryogenic environments. Dense deformation twins and multiple shear bands intersected, forming a weave-like microstructure that can disperse the deformation and benefits energy absorption. Deformation twins can also strengthen the matrix and delay the crack nucleation and growth. While under dynamic loading, an FCC to HCP phase transformation was activated, forming a nano-laminated dual-phase (NLDP) FCC/HCP structure in the matrix, leading to further strengthening and toughening. Deformation twinning and HCP phase transformation act as additional plastic deformation mechanisms along with stacking faults and shear bands to offset the shortcomings caused by limited dislocation movements at low temperatures and high strain rate dynamic loading, enabling the high strength and energy absorption of the syntactic foam.

1. Introduction

Metal foams are widely used in various engineering fields due to their unique characteristics, such as low density, high impact energy absorption, high specific stiffness, damping capacity, etc. [1,2]. These exceptional mechanical and physical properties make metal foams more attractive for lightweight structural, impact protection, and functional applications than their solid counterparts [3–7]. Furthermore, as a promising candidate, metal foams have broad applications in cryogenic engineering, such as liquefied gas industry, outer space exploration, cryogenic superconductivity, etc. [8]. Encouraged by their superior properties and widespread applications, extensive studies have been performed on metal foams. However, most studies were conducted at room temperature, and only a few were focused on performance at extremely low temperatures [9–15].

Kaczyński et al. [12] investigated the energy absorption of four aluminum foams under quasi-static and dynamic compression at cryogenic (−175 °C) and high temperature (750 °C) to explore applying aluminum foams in the liquefied natural gas (LNG) tanks. They found that cryogenic temperature increases energy absorption under quasi-static deformation but does not affect the amount of energy absorbed under dynamic conditions. Fiedler et al. [13] performed compression tests on two metal matrix syntactic foams at room and liquid nitrogen temperature. The results indicate that the zinc alloy (ZA27) syntactic foam exhibits a pronounced embrittlement effect at cryogenic temperature, and the sample collapses in brittle shear fracture mode. In contrast, the aluminum alloy (A356) syntactic foam is less sensitive to this effect. Khezrzadeh et al. [14] examined the anisotropic

* Corresponding author. State Key Laboratory of Nonlinear Mechanics, Institute of Mechanics, Chinese Academy of Sciences (CAS), Beisihuanxi Road, No. 15, Beijing, 100190, PR China.
** Corresponding author. State Key Laboratory of Nonlinear Mechanics, Institute of Mechanics, Chinese Academy of Sciences (CAS), Beijing, 100190, PR China.
E-mail addresses: Chenyan@lnm.imech.ac.cn (Y. Chen), lhdai@lnm.imech.ac.cn (L.-H. Dai).

https://doi.org/10.1016/j.msea.2023.145146
Received 17 January 2023; Received in revised form 8 May 2023; Accepted 10 May 2023
Available online 11 May 2023

compressive behavior of a closed-cell aluminum alloy (A356) foam under three temperatures (−196, 25, and 250 °*C*). It was found that the foam exhibits higher strength when the long axis of the elliptical cells is parallel to the load direction. And due to the ductile-to-brittle transition with temperature decreases, the foam presented a higher strength at −196 °*C* but fractured in a brittle mode. Song et al. [9,16,17] investigated the quasi-static and dynamic compression properties of several lotus-type porous metals (including carbon steels, copper, and iron) with unidirectional cylindrical pores at room (25 °*C*) and cryogenic (−196 °*C*) temperatures. These foams have high strength, but their cylindrical pore structure also endows them with anisotropic mechanical properties. Generally, when the load is parallel to the pore direction, the strength is higher than that perpendicular to the pore direction. As in other studies, samples present higher strength and become more brittle at low temperatures and under dynamic loadings.

Some metal foam matrix composites have also been investigated in the past decades. Linul et al. [11] studied compressive crushing performances of a closed-cell aluminum alloy (AlSi10) foam reinforced with stainless steel mesh at temperatures from −196 to 250 °*C*. They also investigated the axial crashworthiness performance of foam-based composites made of aluminum thin-walled circular tubes filled with aluminum alloy (A356) foam [15]. The results indicate that mechanical properties and deformation mechanisms of foam composites strongly depend on temperature. At cryogenic temperature, foam composites exhibit the highest strength and energy absorption performance. However, the deformation mechanism changes from ductile to brittle as temperature decreases.

The dynamic mechanical response of metal foams has also been extensively studied due to their application as impact protection materials. Movahedi et al. [18,19] studied the dynamic compression response of functionally-graded (FG) metal matrix syntactic foams, which are composed of expanded perlite (EP) filled layer and activated carbon (AC) particles filled layer. They investigated the effects of matrix material (ZA27 and A356), aspect ratio, and impact velocity on the mechanical properties of foams. The failure mechanisms of foams and differences in the deformation process in EP and AC layers were also studied. Liang et al. [20] studied the impact behavior of Al matrix syntactic foams with homogeneous and two types of layered structures. They also established an analytical model for stress and strain evolutions in the foams during impact, which agrees well with the experimental results. Alteneiji et al. [21] systematically studied the quasi-static and dynamic mechanical responses of aluminum matrix syntactic foams (Al7075-T6 matrix with ceramic spheres). Split Hopkinson pressure bar, terminal ballistic impact tests, and blast loading were performed to test the dynamic behavior. They also developed a finite element model to simulate the dynamic response of the foam under compression, ballistic impact, and blast loading and achieved good prediction results.

From the above review of previous studies, it can be seen that the embrittlement of materials is a major challenge in cryogenic applications, and the anisotropy caused by the pore structure is also an issue that can be optimized. Therefore, progresses in these two aspects will broaden the cryogenic application of metal foams.

Selecting alloys with high cryogenic toughness to fabricate metal foams is a good way to solve the embrittlement effects at low-temperature. During the past two decades, a new class of alloys, the high entropy alloys (HEAs), has been developed, offering more options for metallic foam fabrication due to its excellent properties [22–31]. Our previous research developed a CoCrFeMnNi HEA syntactic foam [32], which exhibits high strength and energy absorption capacity at room temperature. The matrix alloy, CoCrFeMnNi HEA, is found to have exceptional fracture toughness values exceeding 200 MPa $m^{1/2}$ at room and cryogenic temperature [33], and its mechanical properties even improve with temperature decreases [34–36]. This is because the stacking fault energy (SFE) of the alloy decreases with lowering the temperature, enabling a transition of deformation mechanism from dislocation planar slip to deformation twinning [34,37–39]. Therefore, the CoCrFeMnNi matrix syntactic foam is promising to overcome the embrittlement effects and has a great potential for cryogenic applications. Moreover, its uniformly distributed spherical pore structure will not cause anisotropy.

The present work systematically investigated the mechanical properties and deformation mechanisms of CoCrFeMnNi syntactic foam at liquid nitrogen temperature (−196 °*C*) under quasi-static and high strain rate dynamic compression. In terms of mechanical properties, the foam exhibits ultra-high strength at −196 °*C*, almost twice that of room temperature, along with exceptional energy absorption capacity. Moreover, an excellent resistance to brittle fracture at cryogenic temperature and high strain rate loading is presented. In addition, investigating the deformation microstructures at cryogenic temperature and different strain rates loading reveals the in-depth mechanisms of its superior properties. It was found that multiple deformation mechanisms were activated, including dislocation slip, twinning, stacking faults, shear bands, and HCP phase transformation. Their progressive synergy compensates for the drawbacks caused by the restricted dislocation motion at cryogenic environments and high strain rate loading, ensuring the matrix's strength and ductility and making the foam perform well in extreme conditions.

2. Materials and methods

2.1. Sample fabrication and mechanical tests

The syntactic foams were fabricated with CoCrFeMnNi ingot and Al_2O_3 cenospheres by gas pressure infiltration in an induction furnace with custom-designed devices. The details of the fabrication process and experimental set-ups were described in our previous work [32,40] and will only be introduced briefly here. We used quartz crucibles with a diameter of 14 mm as the container of the fabrication process. And the inner wall of the crucible was coated with boron nitride to avoid the reaction between melted alloy and SiO_2. First, we put an alumina tube into the crucible, used as a mold. And then, the alumina cenospheres were filled into the alumina tube, and a CoCrFeMnNi alloy ingot was placed on the top. Next, the quartz crucible was installed in the induction furnace, connected with the vacuum pump and the argon gas bomb and evacuated to $\sim 5 \times 10^{-3}$ Pa. After that, we melted the alloy ingot by induction heating. When the molten alloy formed a seal with the quartz crucible, argon gas was introduced rapidly to force the melted alloy to infiltrate the space between the cenospheres. Finally, the assembled apparatus was cooled in the induction furnace, and the syntactic foam was consequently removed from the mold.

Samples for mechanical testing were machined from raw foam ingots with a diamond wire saw. And the ends of the samples were ground with SiC paper to ensure flatness and minimize friction. The dimensions of the cylindrical specimens for compression tests at strain rates of 10^{-3} are 8 mm in diameter and 12 mm in height. And the specimens for dynamic compression tests (2000 s^{-1}) are 6 mm in diameter and 6 mm in height. A smaller specimen diameter is to obtain greater deformation under dynamic loading, and reducing the aspect ratio is to achieve dynamic stress equilibrium soon [41,42]. For comparative analysis with the compression behavior of the foam samples, we also tested the quasi-static and dynamic mechanical properties of the solid matrix alloy at 20 and -196 °*C*. The specimen dimensions for the quasi-static tests are ∅ 4 × 6 mm, and the dynamic tests are ∅ 4 × 4 mm. Three specimens were tested in each group.

Mechanical tests of syntactic foam were performed in accordance with ISO 13314: 2011 standard [43]. Five specimens for each experimental condition were tested to verify the repeatability. All compression tests with different strain rates were carried out at −196 °*C* and 20 °*C* using an electronic universal testing machine (CMT 5105S, 100 kN load cell) and the split Hopkinson pressure bar (SHPB) method [44,45], respectively. For the SHPB tests, high-strength steel bars with a diameter of 12.6 mm were used. The striker bar was 400 mm long, while the

incident bar and transmitter bar were 1000 mm long. For compression tests at strain rates of 10^{-3} s^{-1}, strains were measured by an extensometer attached to the platen. For compression tests at −196 °C, the samples were immersed in a liquid nitrogen bath and kept submerged during the test. Quasi-static compressive tests (10^{-3} s^{-1}) at −196 °*C* were interrupted at strains of 10%, 20%, 30%, 40%, and 50% to investigate deformation and microstructure evolution.

2.2. Microstructural characterization

Longitudinal sections were cut from the deformed foam samples, ground and polished with SiC abrasive papers and then with diamond suspensions. The microstructures and the morphology of deformed syntactic foams were characterized by a scanning electron microscope (SEM, JEOL JSM-7001F). To obtain in-depth microstructure information, we extracted foils from the region of interest of deformed struts with a focused ion beam (FIB, FEI Helios Nanolab 600i) instrument. Furthermore, a transmission electron microscope (TEM, Tecnai G^2 F20 S-TWIN at 200 kV) was used to characterize the deformation microstructures.

3. Results and discussions

3.1. Physical properties, porous structure and microstructures

The physical properties of the foam, such as density, porosity, porous structure and morphology, as well as the microstructure and chemical composition of the matrix, have been reported in our previous work. We refer to Ref. [32] for details. The X-ray diffraction (XRD) patterns of syntactic foam, matrix, and cenospheres are shown in Fig. S1.

3.2. Compressive behavior and energy absorption

Fig. 1 shows the mechanical tests data and photographs of CoCrFeMnNi syntactic foam under quasi-static (10^{-3} s^{-1}) and dynamic (2000 s^{-1}) compression at 20 °*C* and −196 °*C*. The quasi-static compression data at room temperature were retrieved from previous work [32]. The stress-strain curves shown in Fig. 1a are average curves of five sets of data. All four curves exhibit a similar shape, with an initial linear region followed by a continuous ascending stress plateau, exhibiting typical ductile deformation characteristics of metallic foam [46,47]. It can be noted that curves under dynamic compression (both at 20 and -196 °*C*) have a lower strain range. This is due to the limitation of SHPB experimental testing. The loading duration of the sample depends on the length of the striker bar, and the stress amplitude of the incident wave depends on the impact velocity. Under current experimental conditions, we cannot make the sample completely densified. Therefore, the curves shown in Fig. 1a do not mean that the sample can only be compressed to this strain value.

As shown in Fig. 1a, the strength of the CoCrFeMnNi syntactic foam was enhanced at −196 °*C* under both quasi-static and dynamic loading compared to that at 20 °*C*. The most important strength parameter of foam, compressive strength (σ_c), is defined as the first peak stress of the curve. Therefore, the compressive strengths of the foam under quasi-static and dynamic tests at −196 °*C* are 472.1 ± 28.3 and 497.3 ± 24.5 MPa, respectively. These values are much higher than that upon quasi-static and dynamic compression at 20 °*C*, which are 241.5 ± 20.3 and 356.8 ± 20.7 MPa. In addition to compressive strength, the metallic foam has two essential strength parameters: densification strength (σ_d) and plateau stress (σ_p). The σ_d is the stress at the densification strain (ε_d). We define 50% as the densification strain [32], thus the σ_d of the foam

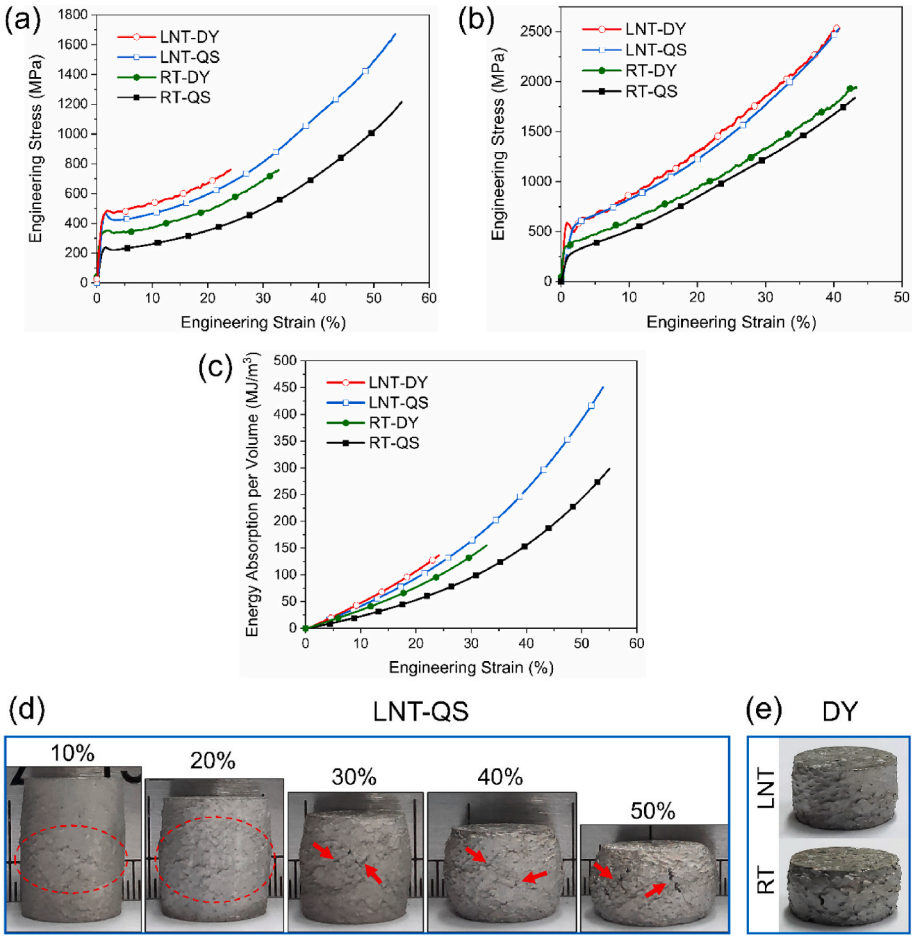

Fig. 1. (a) The average stress-strain curves of CoCrFeMnNi syntactic foams under quasi-static (QS) and dynamic (DY) compression at 20 °*C* (RT) and −196 °*C* (LNT). (b) The representative stress-strain curves of CoCrFeMnNi matrix alloy under quasi-static and dynamic compression at 20 °*C* and −196 °*C*. (c) The EACs as a function of strain of each experimental condition. (d) The photograph of deformed foam samples under quasi-static compression at −196 °*C*. (e) The photograph of deformed foam samples under dynamic compression at −196 °*C* and 20 °*C*.

under quasi-static compression at 20 °C and −196 °C are 1009.0 ± 74.2 and 1490.1 ± 174.2 MPa, respectively. And the σ_p is the average stress over the stress plateau, i.e., from σ_c to σ_d. Accordingly, the σ_p under quasi-static compression at −196 °C and 20 °C are 850.8 ± 57.0 and 497.2 ± 42.0 MPa, respectively. However, due to the limitations of experimental conditions, the dynamically compressed samples did not achieve full densification. Therefore, their plateau stresses are not defined.

For comparison with the syntactic foam, the mechanical properties of the solid CoCrFeMnNi matrix were also tested under quasi-static and dynamic compression at 20 °C and −196 °C. And the representative stress-strain curves of matrix are shown in Fig. 1b. The curves show a linear elastic stage at first, and then the stress increases monotonically with strain. Under each experimental condition, the samples were deformed in a ductile mode and could always withstand compression without fracture, exhibiting excellent toughness. Like syntactic foam samples, the matrix shows higher strength at low temperatures. Meanwhile, the strength under dynamic loading is higher than that under quasi-static loading at the same temperature. However, the strength increase of the matrix under high strain rate loading is smaller than that of the foam, which indicates that the cellular structure could increase the strain rate sensitivity of the material.

The energy absorption capacity (EAC) of syntactic foam under different conditions can be measured from the stress-strain curves according to the equation:

$$W(\varepsilon) = \int_0^{\varepsilon} \sigma(\varepsilon')d\varepsilon' \quad (1)$$

The EACs as a function of strain are plotted in Fig. 1c. For quasi-static compression, we measured the EAC at the densification strain, i.e., $W(50\%)$, which is 389.8 ± 24.4 and 242.8 ± 20.6 MJ/m^3 for the tests at −196 °C and 20 °C. And their energy absorption per mass $W_M(50\%)$ are 78.2 ± 3.1 and 48.6 ± 4.1 kJ/kg, respectively. According to Fig. 1c, the EAC of dynamic compression at −196 °C is higher than that of quasi-static at −196 °C, followed by dynamic compression at 20 °C, and then the quasi-static compression at 20 °C. The mechanical and energy absorption properties are summarized in Table 1.

The samples tested at cryogenic temperature and high strain rate did not show significant embrittlement, which can be reflected in the macroscopic photographs in Fig. 1d and e. It was found that syntactic foams deformed in a diffusive and ductile mode and gradually squashed into a barrel shape. The damage propagates from the pores in the middle to the whole sample. A large number of microcracks generated by the fracture of the cell struts and the collapse of the cell walls intersect each other, forming massive wrinkles on the surface of the specimen (red circles). As the deformation proceeded, multiple small cracks formed but did not penetrate the sample (red arrows), avoiding catastrophic failure caused by a single main crack. This phenomenon indicates that the crack growth is inhibited in the unbroken zone of the sample, which can be attributed to the excellent toughness of the matrix. It is noticed that there are no significant differences in macroscopic deformation between the different temperatures and strain rates, either from the stress-strain curves or the macroscopic photographs.

Table 1
Mechanical properties of CoCrFeMnNi syntactic foams.

Mechanical properties	Units	LNT-QS	LNT-DY	RT-QS	RT-DY
Compressive strength	σ_c/**[MPa]**	472.1 ± 28.3	497.3 ± 24.5	241.5 ± 20.3	356.8 ± 20.7
Densification Strength	σ_d/**[MPa]**	1490.1 ± 174.2		1009.0 ± 74.2	
Plateau Stress	σ_p/**[MPa]**	850.8 ± 57.0		497.2 ± 42.0	
Energy absorption per volume at 50% strain	$W(50\%)$/**[MJ/m^3]**	389.8 ± 24.4		242.8 ± 20.6	
Energy absorption per mass at 50% strain	$W_M(50\%)$/**[kJ/kg]**	78.2 ± 3.1		48.6 ± 4.1	

3.3. Effects of temperature and strain rate on foam properties

It is well known that lowering temperature and increasing strain rate have similar effects on the deformation mechanisms, and their combined effects can be described by Zener-Hollomon parameter [48], $Z = \dot{\varepsilon}\exp(Q/RT)$, where $\dot{\varepsilon}$ and T are the strain rate and absolute temperature, Q is the activation energy, and R is gas constant. At low temperatures, dislocations require more external drive stress to overcome barriers due to less thermal activation; and high strain rates do not allow sufficient time for dislocations to slip and lead to localized dislocation concentration [49]. Therefore, they both make dislocation movement difficult and result in high flow stress.

The effects of strain rate and temperature upon strength can be manifested from the stress-strain curves (Fig. 1a). A strong strain rate effect can be seen at 20 °C. At a high strain rate of 2000 s^{-1}, the strength increases by about 40%. However, this rate effect is decreased at −196 °C. To study the influences of temperature on the strain rate effect, we compared the strain rate sensitivity of syntactic foam and matrix at several strains (5%, 10%, 15%, 20%, and 24%) under different experimental conditions, as shown in Fig. 2. We calculated the strain rate sensitivity (m) at two temperatures from 10^{-3} to 2000 s^{-1} strain rate range, $m = \partial\ln(\sigma)/\partial\ln(\dot{\varepsilon})$, where σ is the flow stress and $\dot{\varepsilon}$ is the strain rate [50]. It can be found that the strain rate sensitivity of both syntactic foam and matrix is reduced at low temperatures. And this decrease in m with lowering temperature has also been found in other research of CoCrFeMnNi matrix [50] and some FCC alloys [51,52]. This phenomenon may be related to the transition of the plastic deformation mechanism as temperature decreases. At room temperature, deformation is dominated by dislocation activity. While at low temperatures, massive deformation twins act as an additional important deformation mechanism. Twins will form when the applied stress reaches the critical resolved shear stress (CRSS) of twinning, and the CRSS is roughly independent of temperature and strain rate [37,50]. With the formation of twins, the local stress is relaxed, so the flow stress does not increase

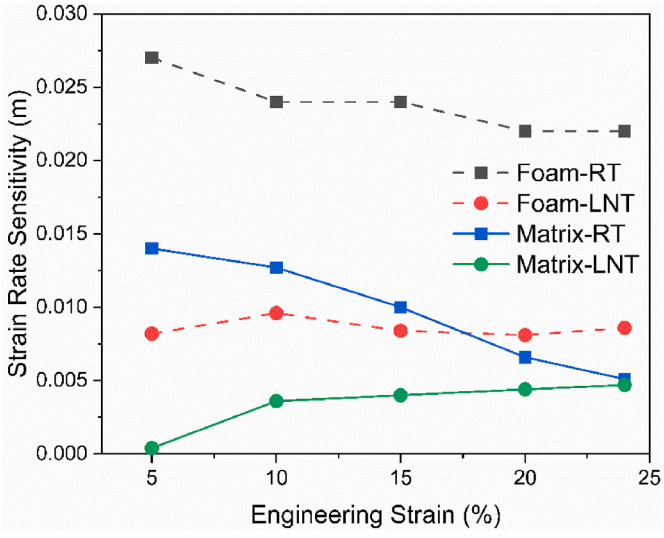

Fig. 2. Strain rate sensitivity of syntactic foam and matrix at room and liquid nitrogen temperature at strains of 5%, 10%, 15%, 20%, and 24%.

significantly with the increase in strain rate. As the proportion of deformation twins increases at low temperatures, the foam becomes more insensitive to strain rate. In addition, the m of syntactic foam is significantly greater than that of the matrix at the same temperature, indicating that the porous structure can increase the strain rate sensitivity.

3.4. Microstructure evolution under quasi-static compression at −196 °C

Fig. 3 shows the SEM micrographs of deformed syntactic foams under quasi-static compression at −196 °C. As shown in Fig. 3a, the deformation is concentrated in a few layers of pores at the early stage (10% strain). In the damaged zone, cell struts bent plastically and fractured subsequently, and cell walls were also broken (Fig. 3b), resulting in cracks propagating into adjacent pores and extending the deformation area. Thanks to the excellent toughness of the matrix, samples maintain ductile deformation even at −196 °C, as evidenced by the plastically bent cell struts. As deformation progresses (40% strain, Fig. 3c and d), most pores have been squashed, and the cell struts are also severely bent or broken. However, these cracks and failures are dispersed in the matrix and not connected to form a large deformation band, thus avoiding catastrophic damage.

To investigate the deformation microstructure evolution, we prepared TEM foil samples by FIB technique from a plastically bent strut of a sample compressed to 10% strain and an area adjacent to a crack of a sample compressed to 50% strain. It is worth mentioning that the nominal compressive strain of the sample is not the same as the actual deformation degree of the struts. We use the microstructure of the plastically bent strut to represent the case of the early deformation stage and the microstructure near the crack to represent the case of the later deformation stage. Fig. 4 shows the bright-field (BF) TEM micrographs of a bent strut, and the sampling area is indicated by the yellow circle in Fig. 3a. The sample has a high density of dislocations, and some fine shear bands can also be observed (red dashed frame area). Fig. 4b exhibits the dislocation configurations by adjusting tilting angles. Highly dense dislocation walls (HDDWs) can be extensively observed in the sample, indicating that deformation at the early stage was dominated by dislocation activities. And the lower stacking faults energy at cryogenic temperatures hinders dislocation cross-slip while facilitating planar slip. The magnified image of the HDDWs and dislocation cells are shown in Fig. 4c, and the inset is the selected area electron diffraction (SAED) pattern of the red circle area.

Fig. 5a exhibits the morphology of the red dashed frame area in Fig. 4a, several parallel dark laths are visible, and some thin shear bands traverse across them. The inset shows the SAED pattern of the lath, showing only one set of patterns, indicating that these laths are not twins but HDDWs. Fig. 5b is the BF image of the same area in (a) but under a different tilting angle to illustrate shear bands clearly. In addition to the thicker one in the lower left corner, some finer bands were also observed. Fig. 5c shows the dark field (DF) image of shear bands, and the inset is the SAED pattern. The spot used to take the DF image is pointed by a red arrow and is close to the twin spot, implying the presence of twin components in the shear band. These observations are indicative of the high twinning activity and shear localization propensity at the early deformation stage at −196 °C. We further investigated the interior structure of the shear band. Fig. 5d is the HRTEM image of the red frame area in (b), showing the internal atomic arrangement of shear band. Massive stacking faults are generated in the shear band, and the remnants of twin and matrix plates can also be detected. Fig. 5e is the close-up view of the yellow dashed frame area in (a), showing the intersection area of HDDW and shear band. A significant shear strain has developed and a kink has formed inside the HDDW. The zoom-in image of this kink is shown in Fig. 5f. And the inset is the high-resolution TEM (HRTEM) image, showing the atomic lattice of the vicinity and core area as indicated by the yellow arrows. In the vicinity, the atomic lattice is distorted and rotated; in the core, the lattice rotation is significant, and the grain orientation has a large deviation between the adjacent area caused by the shear strain, so the atomic lattice is ambiguous without clear contrast.

Fig. 6 shows TEM micrographs of the area near the crack, illustrating the microstructure at the later stage of deformation. Fig. 6(a1) is the SEM image indicating the sampling location (yellow frame) extracted

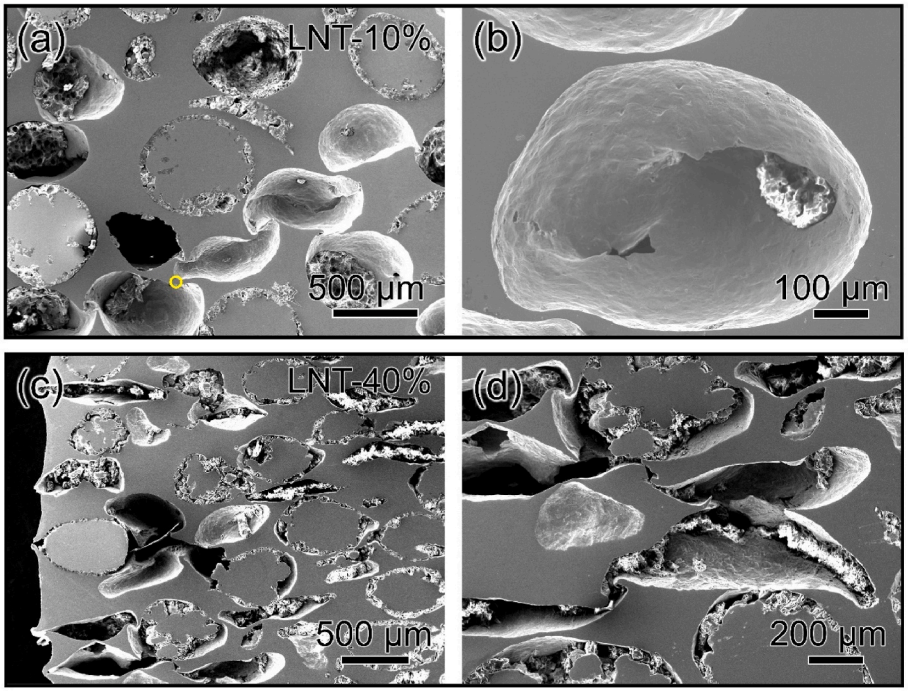

Fig. 3. The SEM images of deformed syntactic foams under quasi-static compression at −196 °C. (a) The deformed sample interrupted at 10% strain. The yellow circle marked the TEM sampling area. (b) The close-up view of a fractured cell wall. (c) The deformed sample interrupted at 40% strain. (d) The magnified morphology of deformed cell struts. (For interpretation of the references to colour in this figure legend, the reader is referred to the Web version of this article.)

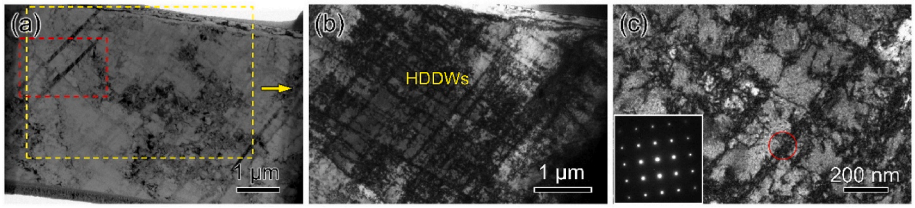

Fig. 4. The TEM bright-field (BF) micrographs of a bent strut under quasi-static compression at −196 °*C*. (a) The low magnification image of the sample. (b) Magnified image under another diffraction condition of the yellow dashed frame area in (a) shows extensive highly dense dislocation walls (HDDWs). (c) The close-up view of HDDWs and dislocation cells, and the inset is the SAED pattern of the red circle area. (For interpretation of the references to colour in this figure legend, the reader is referred to the Web version of this article.)

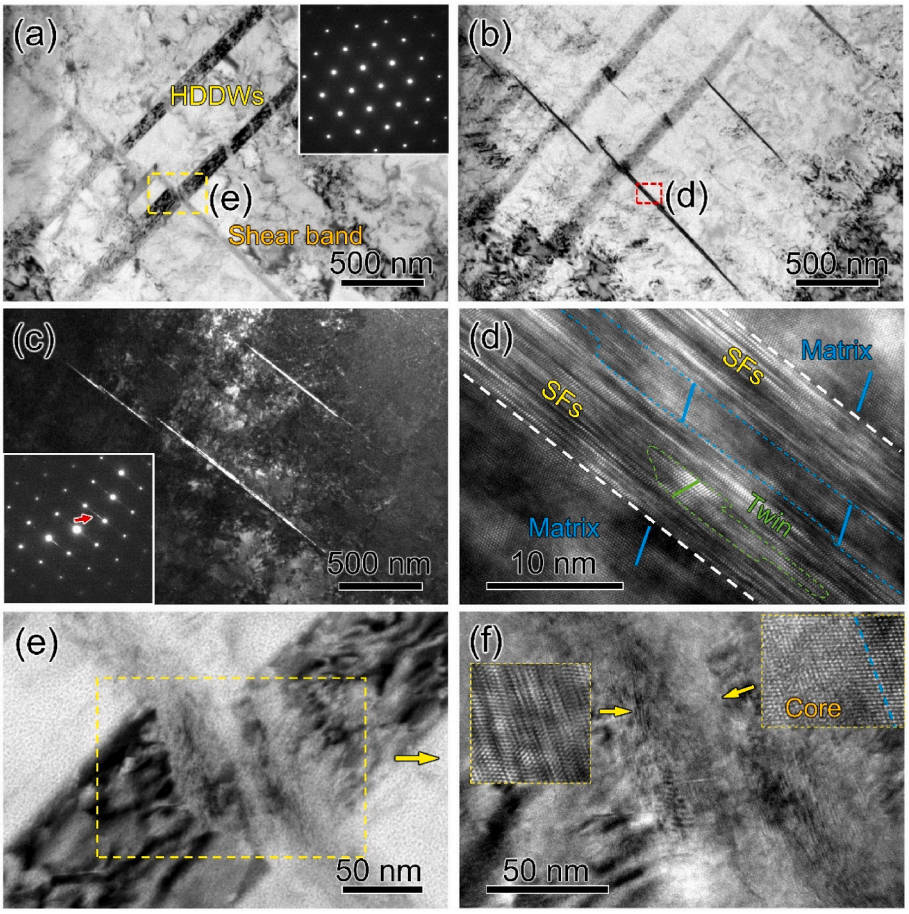

Fig. 5. (a) The BF image of the red dashed frame area of Fig. 4 (a) shows the HDDWs and shear bands. (b) The BF image of the same area in (a) under another diffraction condition. (c) The DF image of (a) and (b) revealing the twins in the shear band. The inset is the SAED pattern, and the arrow indicates the twin spots. (d) The HRTEM image of the red dashed frame area in (b), shows the stacking faults and twin remnants in the shear band. (e) The magnified BF image of the yellow dashed frame area in (a). (f) The zoom-in image of the yellow dashed frame area in (e), and the insets are the HRTEM images of areas pointed by yellow arrows. (For interpretation of the references to colour in this figure legend, the reader is referred to the Web version of this article.)

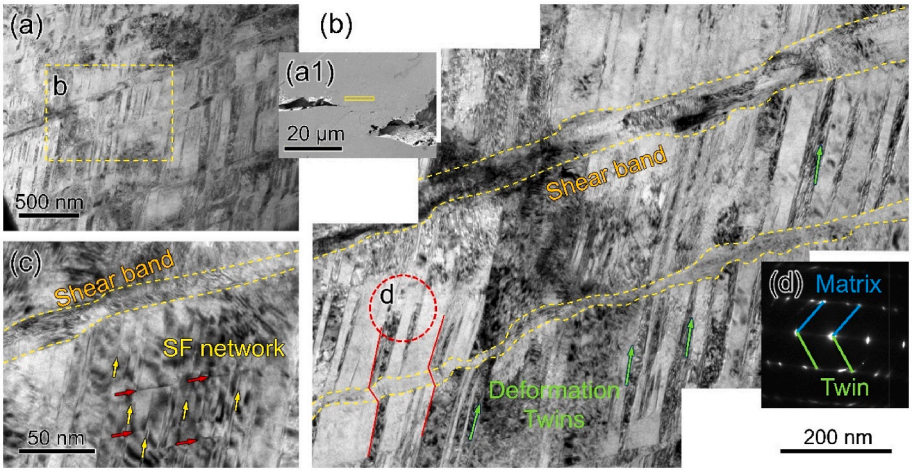

Fig. 6. The TEM micrographs of an adjacent area of crack under quasi-static compression at −196 °*C*. (a) The low magnification BF image showing the DTs and shear bands in the sample. (a1) is the SEM image showing the sampling location. (b) The montage shows the magnified morphology of the shear bands and DTs of the yellow frame area in (a). (c) A magnified BF image shows the stacking faults network near the shear band. (d) The SAED pattern of the red dashed circle area in (b) indicates DTs in the matrix. (For interpretation of the references to colour in this figure legend, the reader is referred to the Web version of this article.)

from a sample under 50% strain compression. TEM characterizations suggest that deformation twins (DTs) serve as an essential mechanism for both plastic deformation and strain hardening upon quasi-static compression at −196 °C. As shown in Fig. 6a, dense DTs are activated in one twinning system, and multiple shear bands propagate through the twin boundaries on another twinning plane. The montage in Fig. 6b exhibits the magnified microstructure of the shear bands and DTs. Fig. 6d shows the SAED patterns of the red circle area in (b), marking the diffraction spots of the matrix and DTs. These DTs act as barriers at the propagating paths of developing shear bands and retard their advance. And the red lines indicate the shear displacements on both sides of DTs after the extending shear band cut through them. Although the shear bands progress through the DT boundaries, a large amount of energy is consumed during their propagation, preventing them from expanding violently. Due to the strengthening on the matrix and the hindering on the shear band propagation brought by DTs, crack nucleation and growth are suppressed, and the foam is protected from brittle fracture. Furthermore, these intersected DTs and shear bands divide the grain into a weave-like structure. In addition, finer microstructure i.e., stacking fault networks also presented in the matrix, as shown in Fig. 6c. These stacking faults in two (111) planes further refine the grains and form a hierarchical weave-like structure together with the intersected DTs and shear bands. This microstructure indicates that more atomic columns are involved in plastic deformation, resulting in a spread-out deformation and consuming more mechanical energy.

The details of DTs, shear bands, and stacking fault networks under quasi-static compression at −196 °C are illustrated further in Fig. 7. Inside the shear band, some recrystallized grains by dislocation activity are visible (Fig. 7a). Dynamic recrystallization is thought to soften the material by reducing the dislocation density [53]. Fig. 7b shows numerous thin primary twins in the matrix and secondary twins inside the shear band. The corresponding diffraction pattern is shown in (b1), demonstrating the existence of twins activated in two twinning systems. In addition, nano stacking fault networks are also visible in the vacant region formed by the intersection of twins and shear bands. These nano stacking fault networks divide the matrix into fine blocks and provide more barriers for dislocation motion that bring strengthening. Moreover, the networks in two orientations also provide more pathways for dislocation glide and cross-slip that accommodate significant plastic deformation [54]. Fig. 7c is the HRTEM image of the red dashed frame area in (b), and the corresponding fast Fourier transformation (FFT) patterns are shown in (c1). It can be seen that primary twins in the matrix pin the boundary of the shear band to restrict its broadening. And secondary twins have evolved within the shear band. In addition, massive stacking faults can be observed near the boundary in the shear band, exhibiting severe deformation in this area. Although stacking faults have a weaker effect on strengthening and strain hardening than twin boundaries [55,56], they are also considered to be barriers to dislocation movement and can accumulate dislocations around them. Therefore, these high density of stacking faults and twins can strengthen the shear band with the deformation proceeds and lead to the self-toughening effects, delaying the crack nucleation caused by material softening.

3.5. Deformation microstructure under dynamic compression at −196 °C and 20 °C

Fig. 8 shows the SEM micrographs of the deformed samples under dynamic compression at −196 °C and 20 °C. Macroscopically, the deformation mode of dynamic compression is similar to that under quasi-static compression, whether at −196 °C or 20 °C. The sample is compressed as the pores fracture gradually, and damages and cracks are dispersed in the matrix, resulting in a diffusive deformation. However, at a smaller scale, the deformation of struts exhibits some differences between quasi-static and dynamic compression at −196 °C. As shown in Fig. 8b and c, the close-up views of the deformed struts reveal that more struts undergo brittle shear fracture, which manifests embrittlement under dynamic compression at −196 °C. Fortunately, the degree of embrittlement is relatively small and does not cause overall brittle failure. Compared to that at −196 °C, the sample deformed at 20 °C exhibits more ductility. More plastically bent struts can be seen in the fractured section (Fig. 8e and f). These observations suggest that increasing strain rate or decreasing temperature alone has little effect on the deformation mode of the foam. However, when both of them act simultaneously, the matrix will embrittle, but it will not cause the overall brittle failure of the foam.

The detailed observations of dynamically deformed microstructure were conducted by TEM, and the sampling locations are marked by the yellow rectangles in Fig. 8c and f. Fig. 9 shows the microstructures of the fractured struts under dynamic compression at −196 °C. In contrast to the weave-like microstructure under quasi-static compression, the dynamically deformed sample exhibits a complex lamellar

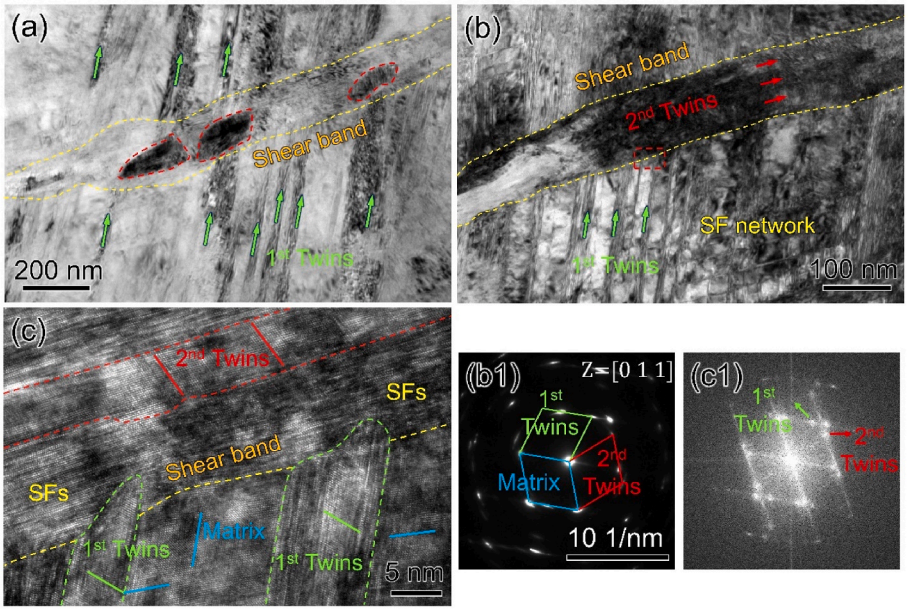

Fig. 7. The detailed characterizations of shear band and DTs under quasi-static compression at −196 °C. (a) The BF image shows the recrystallized grains inside shear band. (b) The BF image of shear band area shows the DTs and stacking faults network. (c) The HRTEM image of the shear band, shows the 1st twins, 2nd twins and stacking faults in the shear band. (b1) is the SAED pattern of (b), shows the diffraction spots of 1st and 2nd twins. (c1) Are the corresponding FFT pattern of (c), also exhibits two sets of twin patterns.

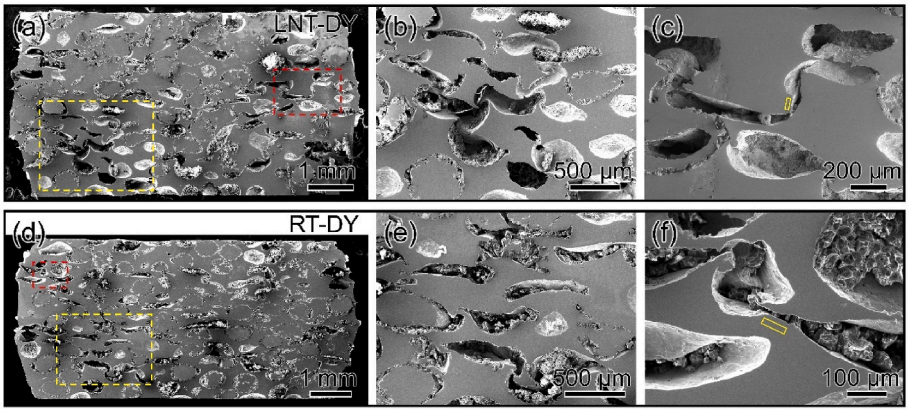

Fig. 8. The SEM images of the syntactic foam deformed under dynamic compression at (a) −196 °*C* and (d) 20 °*C*. (b) and (c) are the close-up views of yellow and red dashed frame area in (a). (e) and (f) are the close-up views of yellow and red dashed frame area in (d), respectively. (For interpretation of the references to colour in this figure legend, the reader is referred to the Web version of this article.)

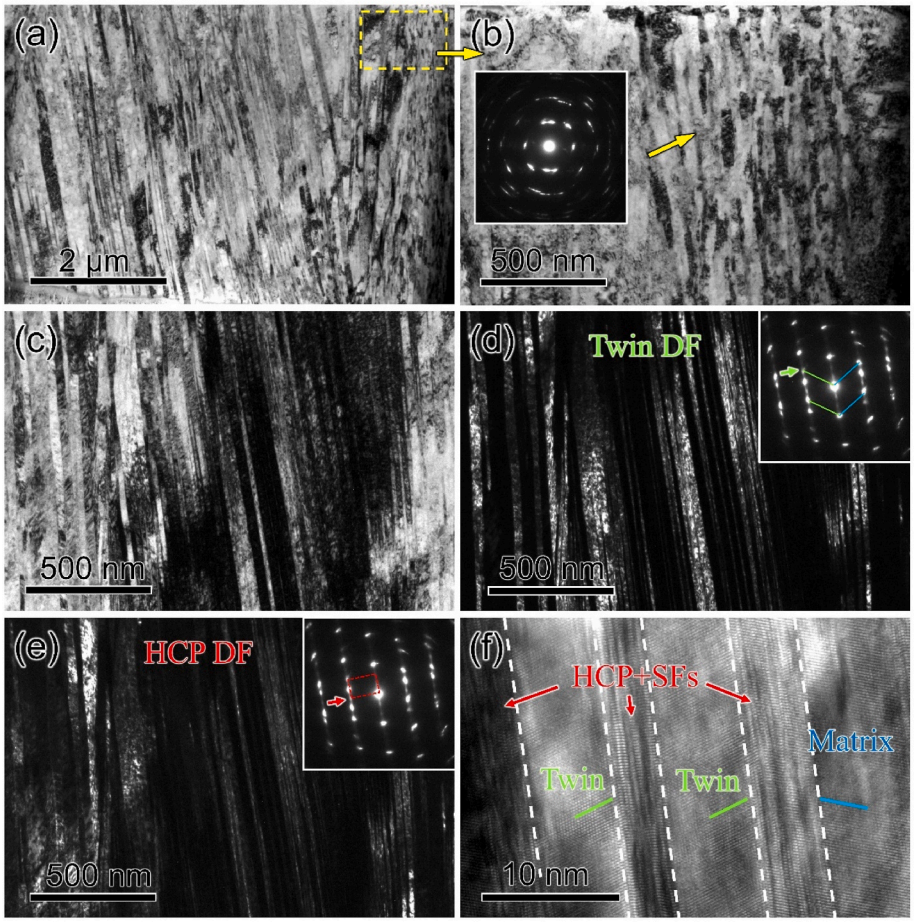

Fig. 9. The TEM characterizations of a fractured strut under dynamic compression at −196 °*C*. (a) The low magnification BF image of the deformed sample. (b) The BF image of the yellow dashed frame area in (a) showing subgrains and dynamic recrystallized grains, inset is the corresponding SAED pattern. (c) The magnified BF image of the lath area mixed with DTs, HCP phases and subgrains. (d) and (e) are the DF image of (c), exhibiting the DTs and HCP phases, and the insets are the corresponding diffraction patterns. (f) The HRTEM image shows the nano-laminated dual-phase FCC/HCP structure. (For interpretation of the references to colour in this figure legend, the reader is referred to the Web version of this article.)

microstructure, consisting of DTs and matrix plates, subgrain laths, and HCP phase plates (Fig. 9a). Fig. 9b is the close-up view of the yellow frame area in (a), revealing the subgrain laths and some dynamic recrystallized grains in the microstructure. The inset is the SAED pattern. The nearly annular patterns demonstrate the existence of subgrains and recrystallized grains, which is an indication of dislocation activities. Fig. 9c–e are the BF and DF images of the lamellar microstructure, and the insets are the corresponding SAED patterns, which reveals that these lamellae are composed of DTs and HCP phases. Meanwhile, the deflection of the spots also indicates the formation of subgrains in the microstructure. However, it is not easy to distinguish them from other lamellae. No HCP phase transition is detected in quasi-static compression, which is unique to dynamic compression. Notably, this deformation-induced HCP phase transformation, along with the DTs, makes the matrix form a nano-laminated dual-phase (NLDP) FCC/HCP structure, which can enhance the mechanical properties [57,58]. Fig. 9f shows the HRTEM image of the NLDP structure. It can be seen that DTs and HCPs lamellae with a width of 5–10 nm are interlaced, and there are massive stacking faults inside them. The role of the NLDP structure on plastic deformation and strengthening will be discussed in detail in the

next section.

Further characterizations of the deformed microstructure revealed other interesting features. Some thin shear bands were found in the lamellae area, as shown in Fig. 10a. Their broadening is constrained by the surrounding lamellae, thus maintaining a small width. Fig. 10b is the HRTEM image, exhibiting the atomic lattice of the shear band and adjacent matrix. The insets are the FFT patterns of the yellow frame areas. Despite the severe deviation and splitting of the spots, two sets of spots can still be distinguished from the pattern of the shear band, as indicated by the red and yellow dashed lines. Furthermore, the orientation relationship of these two sets of patterns is close to the twin relationship. With interactions between dislocations and twin boundaries, the twin boundaries will gradually lose coherency and distort, and the misorientation between the twin and the matrix will increase with the dislocation accommodation. As a result, shear bands continuously evolve during this process. Therefore, these shear bands are also an important plastic deformation carrier under cryogenic and high strain rate loading conditions. In addition to the DTs and HCP lamellae along one direction, there are secondary twins in another twinning plane, as shown in Fig. 10c. Fig. 10d is the HRTEM image, and it is found that there also exists HCP lamella in the secondary twinning plane. Compared to quasi-static compression, these secondary twins are finer and less frequent and therefore play only an auxiliary role in the deformation.

We also characterized the microstructure of the sample under dynamic compression at 20 $^{\circ}C$ for comparison with that at −196 $^{\circ}C$. The TEM BF image (Fig. 11a) exhibits a high density of dislocations and several DTs. Compared with the counterpart deformed at −196 $^{\circ}C$, it has a lower DTs density and finer twin plate width, exhibiting less twinning activities. Furthermore, a closer examination shows some thin dark plates in the DTs, as can be seen clearly in the DF image (Fig. 11b, as pointed by the red arrows in the inset), implying other components in the DTs. We further examined these dark plates and confirmed that they are HCP and matrix plates, as shown in the HRTEM images in Fig. 11c and d. And the corresponding FFT patterns of Fig. 11d are shown in (e). These observations suggest that the HCP phase transformation can occur under dynamic compression at room temperature, and decreasing temperature will promote this process. The lower density and smaller width of the twin and HCP lamellae lead to fewer strengthening effects. Therefore, the foam presents lower strength at 20 $^{\circ}C$.

3.6. Deformation and energy absorption mechanisms at cryogenic temperature and high strain rate

From the above microstructure characterization results, we can see that DTs are activated early and rendered exceptionally profuse as the deformation increases, therefore playing an essential role in the plastic deformation of foam matrix at low temperature. This is due to two reasons. On the one hand, the dislocation slips become difficult at low temperatures. Thus, the flow stress of the material is elevated, allowing the CRSS for twinning (235 ± 10 MPa) [37] to be reached earlier. On the other hand, CoCrFeMnNi alloy has a low SFE of 20–25 mJ/m^2 [59,60] and the SFE decreases with lowering temperature. The temperature-dependent coefficient of SFE ($d\gamma/dT$) for CoCrFeMnNi has been reported to be 0.11 mJ/m^2/K [61]. Therefore, the SFE of CoCrFeMnNi at −196 $^{\circ}C$ is very low and may even close to 0, which promotes deformation twinning. The formation of DTs during the deformation continuously fragments the grain by introducing numerous twin boundaries, which effectively block the motion of dislocations and cause strengthening [34,62–65]. At the same time, this strengthening does not significantly sacrifice plasticity, as reported by several studies of CoCrFeMnNi alloy at low temperatures or under dynamic conditions that DTs simultaneously enhance the strength and plasticity [33,37,66]. As a result, the foam obtains a good synergy of strength and ductility at low temperatures.

It is also worth noting that shear bands are more prone to expand with decreased SFE and elevated driving force at cryogenic temperature. At 20 $^{\circ}C$ [32], shear bands stop expanding after passing through several DTs due to the hindering of twin boundaries. However, at −196 $^{\circ}C$, shear bands break through the twin boundaries continuously and run across the grain (Fig. 6). Although these shear bands propagate to a larger extent, DTs in their expansion path still consume considerable energy to prevent them from expanding violently. In addition, the widening of shear bands is restricted by the pin effects of the primary twins, and the matrix is strengthened by twins and massive stacking fault networks (Fig. 7). As a result, the material softening caused by shear bands is offset, and the evolution of shear bands into cracks is delayed, thus avoiding catastrophic damage. Furthermore, these shear bands also play a favorable role in deformation and energy absorption. These shear bands and DTs fragment the grains in two directions and form a complex weave-like structure. And the resulting formation of numerous interfaces dramatically reduces the dislocation mean free

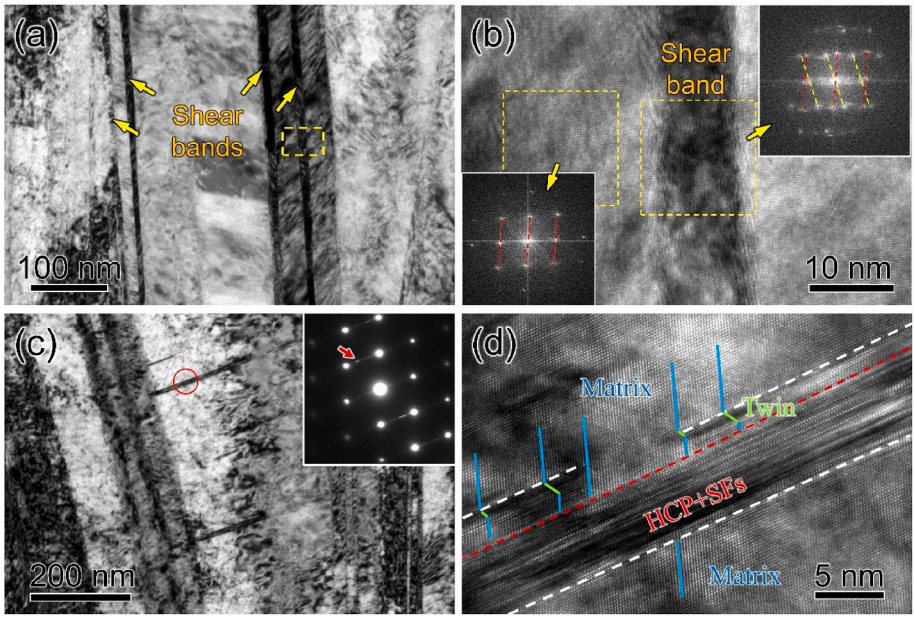

Fig. 10. The TEM observations of shear bands and secondary twins in the deformed sample under dynamic compression at −196 $^{\circ}C$. (a) The BF image shows the thin shear bands parallel to the twin and matrix plates. (b) The HRTEM image of the shear band, and the insets are the FFT patterns of the yellow dashed frame areas. (c) The BF image shows the secondary twins in another twinning system, the inset is the SAED pattern. (d) is the HRTEM image revealing the thin lath in (c) composed of secondary twins and HCP plates. (For interpretation of the references to colour in this figure legend, the reader is referred to the Web version of this article.)

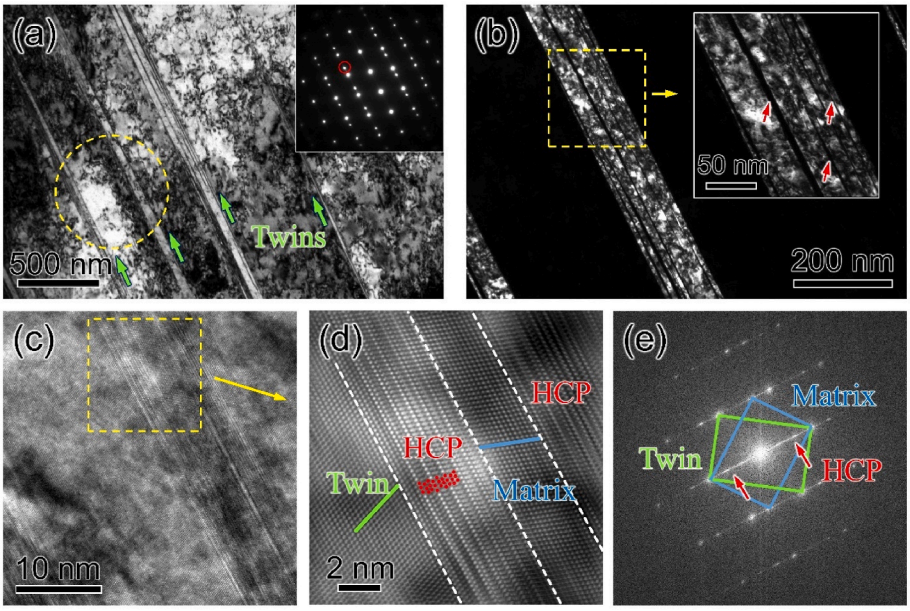

Fig. 11. The TEM characterizations of the sample under dynamic compression at 20 °*C*. (a) The BF image shows the DTs in the matrix, inset is the SAED pattern of the yellow dashed circle area. (b) The DF image of the DTs, the red arrows in the inset indicate the HCP and matrix plates in the DT. (c) and (d) are the HRTEM images of the DT, revealing the HCP and matrix plates in the DT. (e) is the FFT pattern of (d). (For interpretation of the references to colour in this figure legend, the reader is referred to the Web version of this article.)

path and leads to strengthening. Moreover, shear bands and twin boundaries also improve the storage capability of dislocations that could accommodate large plastic deformation. Due to the deformation mechanisms discussed above, the foam presents exceptional mechanical and energy absorption properties under quasi-static compression at cryogenic temperature.

In contrast to quasi-static deformation at −196 °*C*, a NLDP microstructure was observed in the samples under high strain rate loading. It is generally believed that the deformation-induced HCP phase is stronger than the original FCC phase due to its higher Peierls–Nabarro stress and fewer dislocation slip systems [57,67]. Furthermore, the HCP lamellae are very effective barriers to dislocation glide since transmission of edge-component dislocations into the HCP phase would require either ⟨*c*⟩ or ⟨*c* + *a*⟩ dislocations [57,68,69]. These types of dislocation have a very high critical resolved shear stress to activate due to their large Burgers vector [68,70]. Therefore, the HCP lamellae elevate the flow stress of the matrix. In terms of plasticity and ductility, the DTs and HCP lamellae combine the twinning-induced plasticity (TWIP) and transformation-induced plasticity (TRIP) effects, which accommodate significant plastic deformation and provide extensive strain hardening [69,71–74]. The deformation twinning and HCP transformations act as additional plastic deformation mechanisms to compensate for the deficiency caused by the restricted dislocation movement at low temperatures and under dynamic loading [49,75]. Moreover, these twin and phase boundaries impede dislocation motions from one lamella to another that strengthen the matrix and increase the dislocation storage capability, improving strain hardening rate and delaying deformation instability. And these boundaries also allow partial dislocation slip along them to facilitate deformation and improve ductility [76]. Meanwhile, the grain refinement (dynamic Hall-Petch effect) caused by these DTs and HCP phases also contribute to the plasticity and ductility. Therefore, the foam maintains excellent performance under extreme conditions of low temperature and high strain rate loading.

4. Conclusions

The mechanical properties and deformation microstructure of CoCrFeMnNi high entropy alloy syntactic foam under quasi-static and dynamic compression at cryogenic temperature (−196 °*C*) were investigated systematically. The main conclusions can be summarized as follows:

1. The CoCrFeMnNi syntactic foam presents excellent mechanical and energy absorption properties at −196 °*C*. Under quasi-static compression, it has a high strength of 472.1 ± 28.3 MPa and an energy absorption capacity of 389.8 ± 24.4 MJ/m^3. And it exhibits an enhanced strength of 497.3 ± 24.5 MPa and energy absorption capacity under dynamic compression.
2. Under both quasi-static and dynamic compression at −196 °*C*, the syntactic foam deformed in a ductile mode, demonstrating an excellent resistance to embrittlement.
3. A high twinning activity and shear band propagation tendency are observed under quasi-static compression at −196 °*C*. The dense deformation twins and shear bands intersected and formed a weave-like microstructure, leading to a spread-out deformation and more energy absorption.
4. An HCP phase transformation occurred under dynamic compression. These HCP phases accompanied by deformation twins lead to a nano-laminated dual-phase (NLDP) FCC/HCP structure in the matrix, which can enhance the strength and plasticity by combining the twinning-induced plasticity (TWIP) and transformation-induced plasticity (TRIP) effects.

CRediT authorship contribution statement

Jin Meng: Methodology, Formal analysis, Investigation, Writing – original draft, Visualization. **Yu Qiao:** Data curation, Formal analysis. **Yan Chen:** Writing – review & editing, Funding acquisition. **Tian-Wei Liu:** Data curation, Formal analysis. **Tong Li:** Formal analysis. **Hai-Ying Wang:** Writing – review & editing. **Lan-Hong Dai:** Resources, Writing – review & editing, Supervision, Project administration, Funding acquisition.

Declaration of competing interest

The authors declare that they have no known competing financial interests or personal relationships that could have appeared to influence the work reported in this paper.

Data availability

Data will be made available on request.

Acknowledgement

This work is financially supported by the NSFC Basic Science Center Program for "Multiscale Problems in Nonlinear Mechanics" (No.11988102), the NSFC (Nos. 11790292, 11972346, and 12002341), the Ye Qisun Science Foundation of National Natural Science Foundation of China (No. U2141204), and the Key Research Program of the Chinese Academy of Sciences (No. ZDRW–CN–2021-2-3).

Appendix A. Supplementary data

Supplementary data to this article can be found online at https://doi.org/10.1016/j.msea.2023.145146.

References

[1] L.J. Gibson, M.F. Ashby, Cellular Solids: Structure and Properties, 2 ed., Cambridge University Press, Cambridge, 1997 https://doi.org/10.1017/CBO9781139878326.
[2] J. Banhart, Manufacture, characterisation and application of cellular metals and metal foams, Prog. Mater. Sci. 46 (6) (2001) 559–632, https://doi.org/10.1016/S0079-6425(00)00002-5.
[3] F. García-Moreno, Commercial applications of metal foams: their properties and production, Materials 9 (2) (2016) 85.
[4] I.N. Orbulov, Metal matrix composite syntactic foams for light-weight structural materials, reference module in materials science and materials engineering, Elsevier (2021), https://doi.org/10.1016/B978-0-12-803581-8.11918-6.
[5] M.A. Atwater, L.N. Guevara, K.A. Darling, M.A. Tschopp, Solid state porous metal production: a review of the capabilities, characteristics, and challenges, Adv. Eng. Mater. 20 (7) (2018), https://doi.org/10.1002/adem.201700766.
[6] X. Wei, J.H. Chen, L.H. Dai, Energy absorption mechanism of open-cell Zr-based bulk metallic glass foam, Scripta Mater. 66 (10) (2012) 721–724, https://doi.org/10.1016/j.scriptamat.2012.01.039.
[7] H. Lin, H.Y. Wang, C. Lu, L.H. Dai, A metallic glass syntactic foam with enhanced energy absorption performance, Scripta Mater. 119 (2016) 47–50, https://doi.org/10.1016/j.scriptamat.2016.03.034.
[8] L.F. Li, Y.T. Zhang, Y.Y. Li, Chapter 210 - development of cryogenic structural materials, in: L. Zhang, L. Lin, G. Chen (Eds.), Proceedings of the Twentieth International Cryogenic Engineering Conference (ICEC20), Elsevier Science, Oxford, 2005, pp. 885–894, https://doi.org/10.1016/B978-008044559-5/50213-1.
[9] Y.H. Song, M. Tane, H. Nakajima, Peculiar formation mechanism of a plateau stress region during dynamic compressive deformation of porous carbon steel with oriented cylindrical pores, Acta Mater. 60 (3) (2012) 1149–1160, https://doi.org/10.1016/j.actamat.2011.11.001.
[10] T. Dixit, I. Ghosh, Cooling capacity of high porosity open-cell metal foams as passive cryogenic radiators, Cryogenics 84 (2017) 81–88, https://doi.org/10.1016/j.cryogenics.2017.04.005.
[11] E. Linul, L. Marşavina, P.-A. Linul, J. Kovacik, Cryogenic and high temperature compressive properties of metal foam matrix composites, Compos. Struct. 209 (2019) 490–498, https://doi.org/10.1016/j.compstruct.2018.11.006.
[12] P. Kaczyński, M. Ptak, K. Gawdzińska, Energy absorption of cast metal and composite foams tested in extremely low and high-temperatures, Mater. Des. 196 (2020), 109114, https://doi.org/10.1016/j.matdes.2020.109114.
[13] T. Fiedler, K. Al-Sahlani, P.A. Linul, E. Linul, Mechanical properties of A356 and ZA27 metallic syntactic foams at cryogenic temperature, J. Alloys Compd. 813 (2020), 152181, https://doi.org/10.1016/j.jallcom.2019.152181.
[14] O. Khezrzadeh, O. Mirzaee, E. Emadoddin, E. Linul, Anisotropic compressive behavior of metallic foams under extreme temperature conditions, Materials 13 (10) (2020) 2329, https://doi.org/10.3390/ma13102329.
[15] E. Linul, O. Khezrzadeh, Axial crashworthiness performance of foam-based composite structures under extreme temperature conditions, Compos. Struct. 271 (2021), 114156, https://doi.org/10.1016/j.compstruct.2021.114156.
[16] Y.H. Song, M. Tane, H. Nakajima, Dynamic and quasi-static compression of porous carbon steel S30C and S45C with directional pores, Mater. Sci. Eng., A 534 (2012) 504–513, https://doi.org/10.1016/j.msea.2011.11.099.
[17] M. Tane, F. Zhao, Y.H. Song, H. Nakajima, Formation mechanism of a plateau stress region during dynamic compression of porous iron: interaction between oriented cylindrical pores and deformation twins, Mater. Sci. Eng., A 591 (2014) 150–158, https://doi.org/10.1016/j.msea.2013.10.078.
[18] N. Movahedi, T. Fiedler, A. Taşdemirci, G.E. Murch, I.V. Belova, M. Güden, Impact loading of functionally graded metal syntactic foams, Mater. Sci. Eng., A 839 (2022), 142831, https://doi.org/10.1016/j.msea.2022.142831.
[19] N. Movahedi, M. Vesenjak, L. Krstulović-Opara, I.V. Belova, G.E. Murch, T. Fiedler, Dynamic compression of functionally-graded metal syntactic foams, Compos. Struct. 261 (2021), 113308, https://doi.org/10.1016/j.compstruct.2020.113308.
[20] C. Liang, Y. Zhao, Experimental and analytical study on homogeneous and layered Al matrix syntactic foams under impact, Int. J. Impact Eng. 153 (2021), 103861, https://doi.org/10.1016/j.ijimpeng.2021.103861.
[21] M. Alteneiji, K. Krishnan, Z.W. Guan, W.J. Cantwell, Y. Zhao, G. Langdon, Dynamic response of aluminium matrix syntactic foams subjected to high strain-rate loadings, Compos. Struct. 303 (2023), 116289, https://doi.org/10.1016/j.compstruct.2022.116289.
[22] J.-W. Yeh, S.-K. Chen, S.-J. Lin, J.-Y. Gan, T.-S. Chin, T.-T. Shun, C.-H. Tsau, S.-Y. Chang, Nanostructured high-entropy alloys with multiple principal elements: novel alloy design concepts and outcomes, Adv. Eng. Mater. 6 (5) (2004) 299–303, https://doi.org/10.1002/adem.200300567.
[23] B. Cantor, I.T.H. Chang, P. Knight, A.J.B. Vincent, Microstructural development in equiatomic multicomponent alloys, Mater. Sci. Eng., A 375–377 (2004) 213–218, https://doi.org/10.1016/j.msea.2003.10.257.
[24] Z.Q. Fu, L. Jiang, J.L. Wardini, B.E. MacDonald, H.M. Wen, W. Xiong, D.L. Zhang, Y.Z. Zhou, T.J. Rupert, W.P. Chen, E.J. Lavernia, A high-entropy alloy with hierarchical nanoprecipitates and ultrahigh strength, Sci. Adv. 4 (10) (2018) 8, https://doi.org/10.1126/sciadv.aat8712.
[25] Z. Fu, A. Hoffman, B.E. MacDonald, Z. Jiang, W. Chen, M. Arivu, H. Wen, E. J. Lavernia, Atom probe tomography study of an Fe25Ni25Co25Ti15Al10 high-entropy alloy fabricated by powder metallurgy, Acta Mater. 179 (2019) 372–382, https://doi.org/10.1016/j.actamat.2019.08.047.
[26] C. Zhang, C. Zhu, P. Cao, X. Wang, F. Ye, K. Kaufmann, L. Casalena, B. E. MacDonald, X. Pan, K. Vecchio, E.J. Lavernia, Aged metastable high-entropy alloys with heterogeneous lamella structure for superior strength-ductility synergy, Acta Mater. 199 (2020) 602–612, https://doi.org/10.1016/j.actamat.2020.08.043.
[27] Z. Li, S. Zhao, R.O. Ritchie, M.A. Meyers, Mechanical properties of high-entropy alloys with emphasis on face-centered cubic alloys, Prog. Mater. Sci. 102 (2019) 296–345, https://doi.org/10.1016/j.pmatsci.2018.12.003.
[28] P. Shi, R. Li, Y. Li, Y. Wen, Y. Zhong, W. Ren, Z. Shen, T. Zheng, J. Peng, X. Liang, P. Hu, N. Min, Y. Zhang, Y. Ren, P.K. Liaw, D. Raabe, Y.-D. Wang, Hierarchical crack buffering triples ductility in eutectic herringbone high-entropy alloys, Science 373 (6557) (2021) 912, https://doi.org/10.1126/science.abf6986.
[29] W. Li, D. Xie, D. Li, Y. Zhang, Y. Gao, P.K. Liaw, Mechanical behavior of high-entropy alloys, Prog. Mater. Sci. 118 (2021), 100777, https://doi.org/10.1016/j.pmatsci.2021.100777.
[30] X.-F. Liu, Z.-L. Tian, X.-F. Zhang, H.-H. Chen, T.-W. Liu, Y. Chen, Y.-J. Wang, L.-H. Dai, Self-sharpening" tungsten high-entropy alloy, Acta Mater. 186 (2020) 257–266, https://doi.org/10.1016/j.actamat.2020.01.005.
[31] Z. Li, S. Zhao, H. Diao, P.K. Liaw, M.A. Meyers, High-velocity deformation of Al0.3CoCrFeNi high-entropy alloy: remarkable resistance to shear failure, Sci. Rep. 7 (1) (2017), 42742, https://doi.org/10.1038/srep42742.
[32] J. Meng, T.-W. Liu, H.-Y. Wang, L.-H. Dai, Ultra-high energy absorption high-entropy alloy syntactic foam, Compos. B Eng. 207 (2021), 108563, https://doi.org/10.1016/j.compositesb.2020.108563.
[33] B. Gludovatz, A. Hohenwarter, D. Catoor, E.H. Chang, E.P. George, R.O. Ritchie, A fracture-resistant high-entropy alloy for cryogenic applications, Science 345 (6201) (2014) 1153–1158, https://doi.org/10.1126/science.1254581.
[34] F. Otto, A. Dlouhý, C. Somsen, H. Bei, G. Eggeler, E.P. George, The influences of temperature and microstructure on the tensile properties of a CoCrFeMnNi high-entropy alloy, Acta Mater. 61 (15) (2013) 5743–5755, https://doi.org/10.1016/j.actamat.2013.06.018.
[35] Z. Pu, Z.C. Xie, R. Sarmah, Y. Chen, C. Lu, G. Ananthakrishna, L.H. Dai, Spatio-temporal dynamics of jerky flow in high-entropy alloy at extremely low temperature, Phil. Mag. 101 (2) (2021) 154–178, https://doi.org/10.1080/14786435.2020.1822557.
[36] S. Zhao, Z. Li, C. Zhu, W. Yang, Z. Zhang, D.E.J. Armstrong, P.S. Grant, R. O. Ritchie, M.A. Meyers, Amorphization in extreme deformation of the CrMnFeCoNi high-entropy alloy, Sci. Adv. 7 (5) (2021), eabb3108, https://doi.org/10.1126/sciadv.abb3108.
[37] G. Laplanche, A. Kostka, O.M. Horst, G. Eggeler, E.P. George, Microstructure evolution and critical stress for twinning in the CrMnFeCoNi high-entropy alloy, Acta Mater. 118 (2016) 152–163, https://doi.org/10.1016/j.actamat.2016.07.038.
[38] A.S. Tirunilai, T. Hanemann, C. Reinhart, V. Tschan, K.P. Weiss, G. Laplanche, J. Freudenberger, M. Heilmaier, A. Kauffmann, Comparison of cryogenic deformation of the concentrated solid solutions CoCrFeMnNi, CoCrNi and CoNi, Mater. Sci. Eng., A 783 (2020), 139290, https://doi.org/10.1016/j.msea.2020.139290.
[39] I.V. Kireeva, Y.I. Chumlyakov, A.V. Vyrodova, Z.V. Pobedennaya, I. Karaman, Effect of twinning on the orientation dependence of mechanical behaviour and fracture in single crystals of the equiatomic CoCrFeMnNi high-entropy alloy at 77K, Mater. Sci. Eng., A 784 (2020), 139315, https://doi.org/10.1016/j.msea.2020.139315.
[40] J. Meng, Y. Qiao, T.-W. Liu, Y.-Y. Tan, F.-H. Cao, Y. Chen, H.-Y. Wang, L.-H. Dai, Eutectic high entropy alloy syntactic foam, J. Mater. Sci. Technol. 149 (2023) 177–189, https://doi.org/10.1016/j.jmst.2022.12.009.
[41] B. Song, W. Chen, Dynamic stress equilibration in split Hopkinson pressure bar tests on soft materials, Exp. Mech. 44 (3) (2004) 300–312, https://doi.org/10.1007/BF02427897.
[42] B. Song, W. Chen, T. Yanagita, D.J. Frew, Confinement effects on the dynamic compressive properties of an epoxy syntactic foam, Compos. Struct. 67 (3) (2005) 279–287, https://doi.org/10.1016/j.compstruct.2004.07.011.
[43] ISO 13314, 2011 Mechanical Testing of Metals - Ductility Testing - Compression Test for Porous and Cellular Metals, 2011.

[44] H. Kolsky, An investigation of the mechanical properties of materials at very high rates of loading, Proc. Phys. Soc. B 62 (11) (1949) 676–700, https://doi.org/10.1088/0370-1301/62/11/302.
[45] B. Zhang, Y. Lin, S. Li, D. Zhai, G. Wu, Quasi-static and high strain rates compressive behavior of aluminum matrix syntactic foams, Compos. B Eng. 98 (2016) 288–296, https://doi.org/10.1016/j.compositesb.2016.05.034.
[46] G. Castro, S.R. Nutt, Synthesis of syntactic steel foam using mechanical pressure infiltration, Mater. Sci. Eng., A 535 (2012) 274–280, https://doi.org/10.1016/j.msea.2011.12.084.
[47] L. Pan, Y. Yang, M.U. Ahsan, D.D. Luong, N. Gupta, A. Kumar, P.K. Rohatgi, Zn-matrix syntactic foams: effect of heat treatment on microstructure and compressive properties, Mater. Sci. Eng., A 731 (2018) 413–422, https://doi.org/10.1016/j.msea.2018.06.072.
[48] C. Zener, J.H. Hollomon, Effect of strain rate upon plastic flow of steel, J. Appl. Phys. 15 (1) (1944) 22–32, https://doi.org/10.1063/1.1707363.
[49] P. Gao, Z. Ma, J. Gu, S. Ni, T. Suo, Y. Li, M. Song, Y.-W. Mai, X. Liao, Exceptional high-strain-rate tensile mechanical properties in a CrCoNi medium-entropy alloy, SCIENCE CHINA Materials 65 (2095–8226) (2022) 811, https://doi.org/10.1007/s40843-021-1798-6.
[50] J. Moon, S.I. Hong, J.W. Bae, M.J. Jang, D. Yim, H.S. Kim, On the strain rate-dependent deformation mechanism of CoCrFeMnNi high-entropy alloy at liquid nitrogen temperature, Materials Research Letters 5 (7) (2017) 472–477, https://doi.org/10.1080/21663831.2017.1323807.
[51] H. Li, H. Choo, P.K. Liaw, The effect of temperature on strain rate sensitivity in a nanocrystalline Ni–Fe alloy, J. Appl. Phys. 101 (6) (2007), 063536, https://doi.org/10.1063/1.2711411.
[52] Y.M. Wang, A.V. Hamza, E. Ma, Temperature-dependent strain rate sensitivity and activation volume of nanocrystalline Ni, Acta Mater. 54 (10) (2006) 2715–2726, https://doi.org/10.1016/j.actamat.2006.02.013.
[53] Z. Li, S. Zhao, S.M. Alotaibi, Y. Liu, B. Wang, M.A. Meyers, Adiabatic shear localization in the CrMnFeCoNi high-entropy alloy, Acta Mater. 151 (2018) 424–431, https://doi.org/10.1016/j.actamat.2018.03.040.
[54] X. Liu, L. Sun, L. Zhu, J. Liu, K. Lu, J. Lu, High-order hierarchical nanotwins with superior strength and ductility, Acta Mater. 149 (2018) 397–406, https://doi.org/10.1016/j.actamat.2018.01.047.
[55] L. Lu, Z.S. You, K. Lu, Work hardening of polycrystalline Cu with nanoscale twins, Scripta Mater. 66 (11) (2012) 837–842, https://doi.org/10.1016/j.scriptamat.2011.12.046.
[56] L. Zhu, S. Qu, X. Guo, J. Lu, Analysis of the twin spacing and grain size effects on mechanical properties in hierarchically nanotwinned face-centered cubic metals based on a mechanism-based plasticity model, J. Mech. Phys. Solid. 76 (2015) 162–179, https://doi.org/10.1016/j.jmps.2014.12.001.
[57] C. Huang, Y. Yao, X. Peng, S. Chen, Plastic deformation and strengthening mechanism of FCC/HCP nano-laminated dual-phase CoCrFeMnNi high entropy alloy, Nanotechnology 32 (50) (2021), 505724, https://doi.org/10.1088/1361-6528/ac2980.
[58] K. Ming, B. Li, L. Bai, P. Jiang, X. Wu, S. Zheng, J. Wang, Dynamically reversible shear transformations in a CrMnFeCoNi high-entropy alloy at cryogenic temperature, Acta Mater. 232 (2022), 117937, https://doi.org/10.1016/j.actamat.2022.117937.
[59] A.J. Zaddach, C. Niu, C.C. Koch, D.L. Irving, Mechanical properties and stacking fault energies of NiFeCrCoMn high-entropy alloy, J. Occup. Med. 65 (12) (2013) 1780–1789, https://doi.org/10.1007/s11837-013-0771-4.
[60] S. Huang, W. Li, S. Lu, F. Tian, J. Shen, E. Holmström, L. Vitos, Temperature dependent stacking fault energy of FeCrCoNiMn high entropy alloy, Scripta Mater. 108 (2015) 44–47, https://doi.org/10.1016/j.scriptamat.2015.05.041.
[61] S. Zhao, G.M. Stocks, Y. Zhang, Stacking fault energies of face-centered cubic concentrated solid solution alloys, Acta Mater. 134 (2017) 334–345, https://doi.org/10.1016/j.actamat.2017.05.001.
[62] Y. Qiao, Y. Chen, F.-H. Cao, H.-Y. Wang, L.-H. Dai, Dynamic behavior of CrMnFeCoNi high-entropy alloy in impact tension, Int. J. Impact Eng. 158 (2021), 104008, https://doi.org/10.1016/j.ijimpeng.2021.104008.
[63] S. Zhao, R. Zhang, Q. Yu, J. Ell, R.O. Ritchie, A.M. Minor, Cryoforged nanotwinned titanium with ultrahigh strength and ductility, Science 373 (6561) (2021) 1363–1368, https://doi.org/10.1126/science.abe7252.
[64] S. Zhao, R. Zhang, Y. Chong, X. Li, A. Abu-Odeh, E. Rothchild, D.C. Chrzan, M. Asta, J.W. Morris, A.M. Minor, Defect reconfiguration in a Ti–Al alloy via electroplasticity, Nat. Mater. 20 (4) (2021) 468–472, https://doi.org/10.1038/s41563-020-00817-z.
[65] J. Moon, O. Bouaziz, H.S. Kim, Y. Estrin, Twinning engineering of high-entropy alloys: an exercise in process optimization and modeling, Mater. Sci. Eng., A 822 (2021), 141681, https://doi.org/10.1016/j.msea.2021.141681.
[66] Z. Pu, Y. Chen, L.H. Dai, Strong resistance to hydrogen embrittlement of high-entropy alloy, Mater. Sci. Eng., A 736 (2018) 156–166, https://doi.org/10.1016/j.msea.2018.08.101.
[67] S. Chen, H.S. Oh, B. Gludovatz, S.J. Kim, E.S. Park, Z. Zhang, R.O. Ritchie, Q. Yu, Real-time observations of TRIP-induced ultrahigh strain hardening in a dual-phase CrMnFeCoNi high-entropy alloy, Nat. Commun. 11 (1) (2020) 826, https://doi.org/10.1038/s41467-020-14641-1.
[68] Y. Ma, M. Yang, F. Yuan, X. Wu, Deformation induced hcp nano-lamella and its size effect on the strengthening in a CoCrNi medium-entropy alloy, J. Mater. Sci. Technol. 82 (2021) 122–134, https://doi.org/10.1016/j.jmst.2020.12.017.
[69] L. Ding, A. Hilhorst, H. Idrissi, P.J. Jacques, Potential TRIP/TWIP coupled effects in equiatomic CrCoNi medium-entropy alloy, Acta Mater. 234 (2022), 118049, https://doi.org/10.1016/j.actamat.2022.118049.
[70] J.C. Williams, R.G. Baggerly, N.E. Paton, Deformation behavior of HCP Ti-Al alloy single crystals, Metall. Mater. Trans. 33 (3) (2002) 837–850, https://doi.org/10.1007/s11661-002-0153-y.
[71] Y. Qiao, F.-H. Cao, Y. Chen, H.-Y. Wang, L.-H. Dai, Impact tension behavior of heavy-drawn nanocrystalline CoCrNi medium entropy alloy wire, Mater. Sci. Eng., A 856 (2022), 144041, https://doi.org/10.1016/j.msea.2022.144041.
[72] J.-X. Chen, Y. Chen, J.-P. Liu, T.-W. Liu, L.-H. Dai, Anomalous size effect in micron-scale CoCrNi medium-entropy alloy wire, Scripta Mater. 199 (2021), 113897, https://doi.org/10.1016/j.scriptamat.2021.113897.
[73] J.T. Benzing, W.A. Poling, D.T. Pierce, J. Bentley, K.O. Findley, D. Raabe, J. E. Wittig, Effects of strain rate on mechanical properties and deformation behavior of an austenitic Fe-25Mn-3Al-3Si TWIP-TRIP steel, Mater. Sci. Eng., A 711 (2018) 78–92, https://doi.org/10.1016/j.msea.2017.11.017.
[74] M. Wang, Z. Li, D. Raabe, In-situ SEM observation of phase transformation and twinning mechanisms in an interstitial high-entropy alloy, Acta Mater. 147 (2018) 236–246, https://doi.org/10.1016/j.actamat.2018.01.036.
[75] D. Liu, Q. Yu, S. Kabra, M. Jiang, P. Forna-Kreutzer, R. Zhang, M. Payne, F. Walsh, B. Gludovatz, M. Asta, A.M. Minor, E.P. George, R.O. Ritchie, Exceptional fracture toughness of CrCoNi-based medium- and high-entropy alloys at 20 kelvin, Science 378 (6623) (2022) 978–983, https://doi.org/10.1126/science.abp8070.
[76] Z. Zhang, H. Sheng, Z. Wang, B. Gludovatz, Z. Zhang, E.P. George, Q. Yu, S.X. Mao, R.O. Ritchie, Dislocation mechanisms and 3D twin architectures generate exceptional strength-ductility-toughness combination in CrCoNi medium-entropy alloy, Nat. Commun. 8 (1) (2017), 14390, https://doi.org/10.1038/ncomms14390.